

Supplementary Information for

Enhanced Stimuli-Responsive Phase Change Gels through Pickling-Enabled Ion Permeation

Peimin Yu^{1,4}, Xiong Wang^{2,4}, Ziyi Ling^{1,3,*}, Xiaoming Fang^{1,3,*}, Zhengguo Zhang^{1,3}, Steven Wang^{2,*}

Correspondence to: zyiling@scut.edu.cn (Z. L.); xmfang@scut.edu.cn (X. F.);
steven.wang@cityu.edu.hk (S. W.)

This PDF file includes:

Supplementary Methods

Supplementary Notes 1 to 3

Supplementary Figs. 1 to 21

Supplementary Tables 1 to 7

Captions for Supplementary Videos 1 to 4

References

Other Supplementary Materials for this manuscript include the following:

Supplementary Videos 1 to 4

Supplementary Methods

Preparation of PVA/Alg hydrogels

This study utilized a freeze-thaw method¹ to prepare hydrogels, with the specific steps outlined in Supplementary Fig. 1. First, PVA was dispersed in deionized water, heated, and stirred in a water bath at 90 °C for 2 hours to ensure complete dissolution. Then, Alg was added, and the mixture was stirred for an additional 3 hours at 90 °C to form a homogeneous solution. After stopping the stirring, the mixture was removed from the water bath, cooled to room temperature, and poured into silicone molds (diameter 18 mm, height 20 mm). Finally, the samples were frozen at -20 °C for 8 hours and then thawed at 25 °C for 4 hours. This freeze-thaw cycle was repeated three times to obtain form-stable hydrogels. Maintaining a constant water content of 90 wt%, a series of samples was prepared by varying the mass ratio of PVA to Alg to 10/0, 9/1, 8/2, 7/3, 6/4, and 5/5. These samples were named 10P0A, 9P1A, 8P2A, 7P3A, 6P4A, and 5P5A, respectively. The composition of each sample is detailed in Supplementary Table 1.

Measurement of water content in hydrogels

The water content of the hydrogels with various mass ratios of PVA/Alg were listed in Supplementary Table 1. The water content of the hydrogels was calculated by comparing their weight before and after freeze-drying using Equation (S1). Herein, $m_{Hydrogel}$ represents the mass of the hydrogel after being immersed in deionized water for 24 hours to ensure complete swelling. $m_{Aerogel}$ is the mass of aerogel, which is obtained by freeze-drying the swollen hydrogel for 48 hours to remove water.

$$C_{H_2O} = (m_{Hydrogel} - m_{Aerogel}) / m_{Hydrogel} \times 100\% \quad (S1)$$

Measurement of the theoretical content of SAT in PCGs

The theoretical content of SAT (C_{SAT}) is calculated using the mass different of hydrogel before and after pickling. First, record the mass of the hydrogel before pickling as $m_{Hydrogel}$. After being pickled, weigh the mass of obtained PCGs and denote it as m_{PCG} . Based on the water content listed in Supplementary Table 1, the mass of the gel skeleton can be calculated using Equation (S2):

$$m_{gel} = m_{Hydrogel} \times (1 - C_{H_2O}) \quad (S2)$$

The mass of the aqueous solution in the phase change gel is then calculated by subtracting the mass of the dry gel from the mass of the phase change gel, as shown in Equation (S3):

$$m_{aq} = m_{PCG} - m_{gel} \quad (S3)$$

Assuming that the ion permeation process has reached equilibrium, the mass ratio of SA to water in the absorbed salt solution within the three-dimensional network is equal to R . Therefore, the mass of SA in the PCG can be calculated by Equation (S4):

$$m_{SA} = m_{aq} \times \frac{R}{R + 1} \quad (S4)$$

Given the molar masses of SA (M_{SA}) and SAT (M_{SAT}) as 82.03 g/mol and 136.08 g/mol, respectively, the mass of SAT (m_{SAT}) can be calculated using Equation (S5):

$$m_{SAT} = M_{SAT} \times \frac{m_{SA}}{M_{SA}} \quad (S5)$$

Finally, the theoretical C_{SAT} in the PCGs can be calculated by Equation (S6):

$$C_{SAT} = \frac{m_{SAT}}{m_{PCG}} \times 100\% \quad (S6)$$

Crystallinity of PVA

The crystallinity of PVA was determined using differential scanning calorimetry (DSC, TA, Q20). The sample was heated from 225 °C to 350 °C at a rate of 10 °C/min.

Shape stability and leakage resistance test

To assess the form stability and leakage prevention capabilities of the PCGs, a leakage test was conducted. Each PCG specimen was placed on filter paper and subjected to heating at 80°C for 2 hours in an oven. The evaluation included comparing the specimen's shape before and after heating and examining the filter paper for any signs of leakage.

Porosity

Porosity percentages of hydrogels and PCGs were calculated based on their SEM images using the image analysis software package ImageJ. Three images were used for each calculation.

Structural Characterization

The crystallographic structure of PCGs was analyzed using X-ray diffraction (XRD, Bruker, D8 ADVANCE). The PCG samples were cut into 2 × 2 cm² rectangles for the analysis.

Dynamic Mechanical Analysis

Dynamic mechanical analysis (DMA, TA, Q800) was performed in double-cantilever mode at a heating/cooling rate of 2 °C/min and at a frequency of 1 Hz. The sample dimensions were approximately 50 mm × 10 mm × 5 mm.

Three-Point bending test

The samples, measuring 10 mm × 4 mm × 100 mm, were tested using a Universal Testing Machine (Jinan Sida, WDW-10E, 10 kN) under three-point bending testing conditions.

Supplementary Note 1 | Effect of hydrogel microstructure on the thermal and mechanical properties of PCGs

The chemical composition and content significantly affect the structure and properties of hydrogels². Changes in the structure and properties of the parent hydrogel ultimately influence the characteristics of the resulting hydrated salt phase change gels (PCGs). To identify an optimal matrix hydrogel for sodium acetate trihydrate (SAT), a series of hydrogel samples with varying ratios of polyvinyl alcohol (PVA) and sodium alginate (Alg) was systematically prepared. Herein, the mass fraction of deionized water (DI) was held constant at 90 wt%, while the PVA mass fraction ranged from 10 wt% to 5 wt%. The comprehensive preparation process for these hydrogels is detailed in the Supplementary Methods. Subsequently, these hydrogels were immersed in a sodium acetate (SA) solution with a mass ratio of SA to H₂O (*R*) of 1.52 at 80 °C for 48 h, yielding a series of samples denoted as SAT@#P#A, where #P represents the weight percentage of PVA, and #A represents the weight percentage of Alg in the hydrogel.

The PCGs can mold into various shapes, as demonstrated in Supplementary Fig. 2. Moreover, after heating at 80 °C, a temperature exceeding the melting point of SAT, for 2 hours, they maintain their structural integrity. Notably, only sample G (SAT@5P5A) exhibited minor leakage after heating, manifesting as liquid traces on the filter paper. This leakage in SAT@5P5A can be explained by examining the microstructure of the hydrogels and PCGs. As illustrated in Supplementary Fig. 3, a decrease in the proportion of PVA and an increase in Alg result in a noticeable enlargement of the pore diameter within the 3D network. The porosity, derived from the SEM images, steadily increases from 39.1% for Hydrogel 10P0A to 69.5% for Hydrogel 5P5A (Supplementary Fig. 5). This increase in pore diameter is attributed to the reduced crosslink density of the PVA network. The appropriate enlargement of pore size increases the capacity for water absorption. As shown in Supplementary Fig. 5, when the mass ratio of PVA to Alg changes from 10/0 to 6/4, the water content increases from 90.3% to 94.2%. However, when it reaches 5/5, the water content drops to 90.6% due to the weaker interaction force with H₂O. This is caused by the greater distance between the H₂O molecules and the polymer chains resulting from the larger pore size.

After submerging the hydrogel in the sodium acetate (SA) solution, sodium acetate trihydrate (SAT) forms within the hydrogel network and fills their pores (see Supplementary Fig. 3). This results in a steady increase in enthalpy from 198.7 kJ/kg (SAT@10P0A) to 222.6 kJ/kg (SAT@6P4A) (Supplementary Table 2). However, the enthalpy of SAT@5P5A is lower than that of SAT@6P4A (209.8 kJ/kg) and there are many pores observed in its SEM image. These results indicate that the ratio of polyvinyl alcohol (PVA) to sodium alginate (Alg) affects the pore size of the hydrogel and its ability to absorb SAT. Furthermore, we found that the addition of Alg enhances the thermal cyclic stability of PCGs. Comparing the enthalpy loss rate of PCGs after 100 thermal cycles, the loss rate of SAT@10P0A is 14.5%, whereas the loss rate of PCGs with Alg is not higher than 2.6% (Supplementary Table 3). The high loss rate of SAT@10P0A is due to the distinct property of PVA, which forms more hydrophobic crystallization regions during freeze-thaw cycles. In contrast, Alg does not form such regions thereby helping maintain the overall hydrophilicity of the hydrogels. Besides, the combination of SAT with a polymer network has a limited influence on the thermal conductivity of SAT. The conductivity of all samples is around 0.6 W/(m·K), as shown in Supplementary Fig. 4.

The structure of hydrogels influences the mechanical properties of PCGs, in addition to their thermal properties. As shown in Supplementary Fig. 6, the elongation at break and tensile strength of hydrogels decreases as the PVA content, the sole crosslinking network in the PVA/Alg hydrogel, decreases. However, the Young's modulus initially increases and then decreases, with Hydrogel 8P2A exhibiting the highest Young's modulus of 0.15 MPa. This is because the appropriate filling of Alg in the PVA network increases the number of hydrogen bonds in the system, making it relatively difficult to deform. After obtaining PCGs from these hydrogels, the corresponding PCGs demonstrated superior mechanical strength compared to their hydrogel counterparts. Notably, the tensile strength of hydrogels generally remains below 1 MPa, whereas the PCGs exhibited a significant order of magnitude enhancement. The augmentation in Young's modulus is also remarkable, with hydrogels typically having a Young's modulus of approximately 0.1 MPa, while PCGs in their supercooled state exhibited values around 5 MPa. An intriguing observation is that the variation in mechanical properties of PCGs

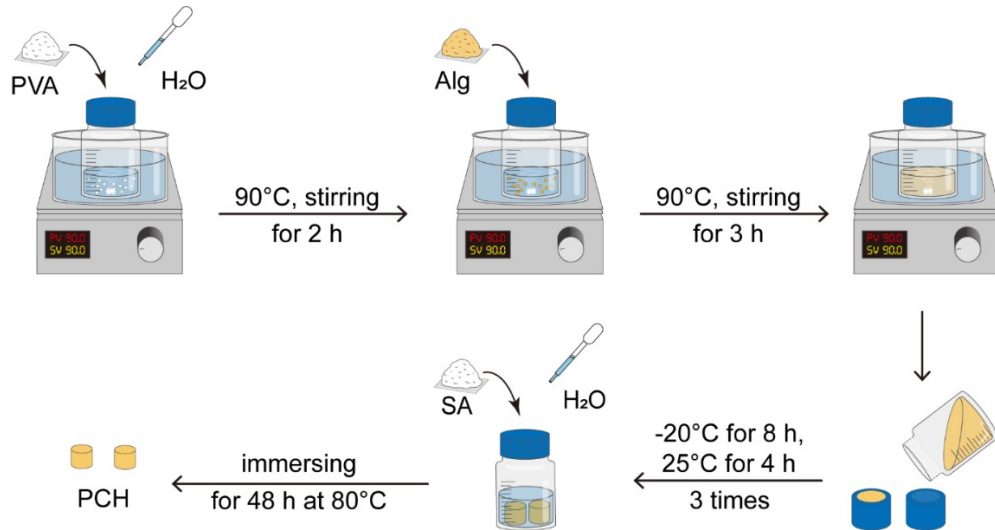
with the mass ratio of PVA/Alg mirrors that of hydrogels. A decrease in PVA content results in reduced network crosslinking density, leading to a weaker network. However, this reduction provides more space to accommodate SAT, resulting in a higher thermal storage capacity. Consequently, to strike a balance between thermal storage capacity and mechanical strength, Hydrogel 8P2A was selected for a more in-depth exploration of the influence of salt concentration.

Supplementary Note 2 | Optimization of the Preparation Method

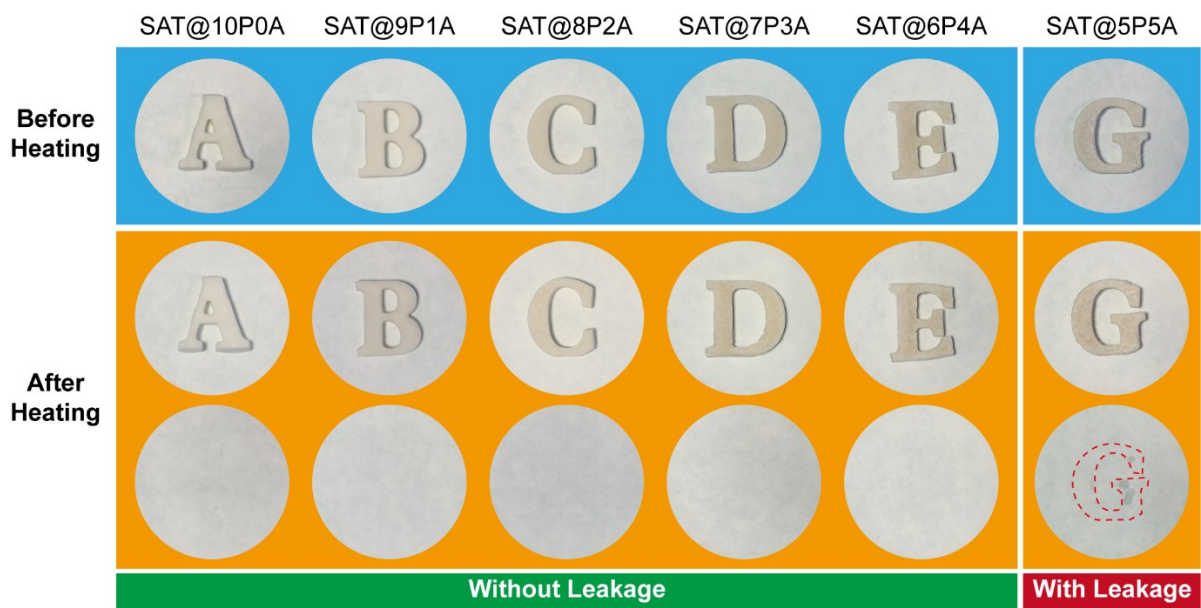
The preparation of PCGs consists of two main steps: hydrogel fabrication and ion-permeation. Both of these steps can be optimized to reduce the overall processing time. For the hydrogel preparation, as shown in Supplementary Table 7, reducing the freeze–thaw cycles from three to one for the 8P2A formulation shortens the fabrication time by 24 hours. This adjustment results in only a slight decrease in tensile strength (from 2.05 MPa to 1.89 MPa), while the phase-change enthalpy notably increases from 210.3 kJ/kg to 222.0 kJ/kg. This shows that a reduction in freeze-thaw cycles can provide a balance between fabrication time and the desired material properties. In addition to optimizing the hydrogel preparation, we are exploring ways to accelerate the ion-permeation process to further shorten the overall production time of PCGs. We will continue to investigate potential strategies for optimizing both steps and improving the efficiency of the process.

Supplementary Note 3 | Lithium-ion battery thermal management performance of PCG-1.52.

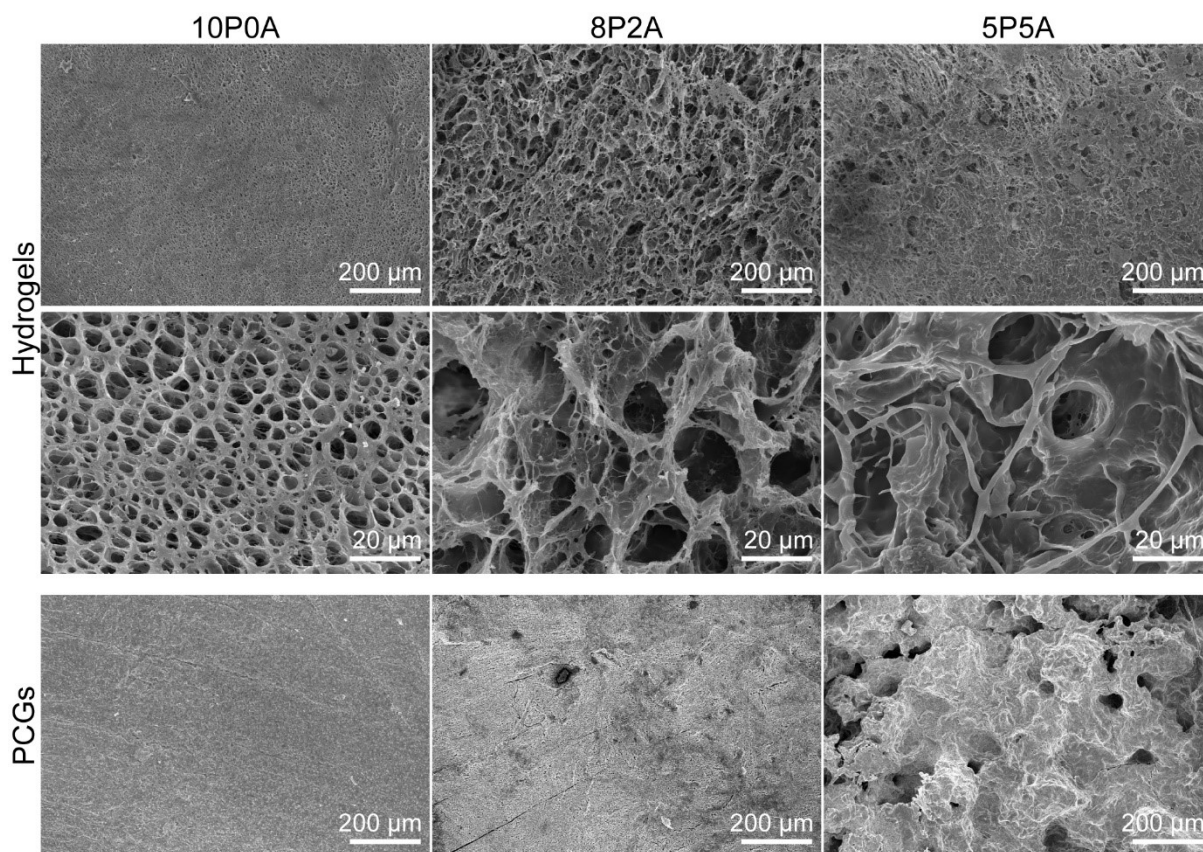
The crystallized-to-melting transition of PCGs enables them to absorb latent heat of up to 210.3 kJ/kg at approximately 56°C, making them highly effective for lithium-ion battery thermal management. To demonstrate this, a single 18650 cell was wrapped with a 2 mm-thick PCG-1.52 sheet (62.5 × 65 mm), and four such cells were arranged in parallel to form a PCG-integrated battery pack. A control group, using the same configuration but without the PCG (with 4 mm spacing between cells), was also assembled for comparison. Under various discharge rates, the control pack exceeded 65°C at a 2.5 C discharge rate and reached 78.7°C at 3 C (Supplementary Fig. 21a). In contrast, the PCG-wrapped pack maintained temperatures below 60°C even at the 3 C discharge rate, reducing the maximum temperature rise within the battery pack by 24.3% (Supplementary Fig. 21b). Additionally, the temperature rise became notably more gradual as it approached the melting point of the PCG (~56°C), further indicating the PCG's effective cooling performance.



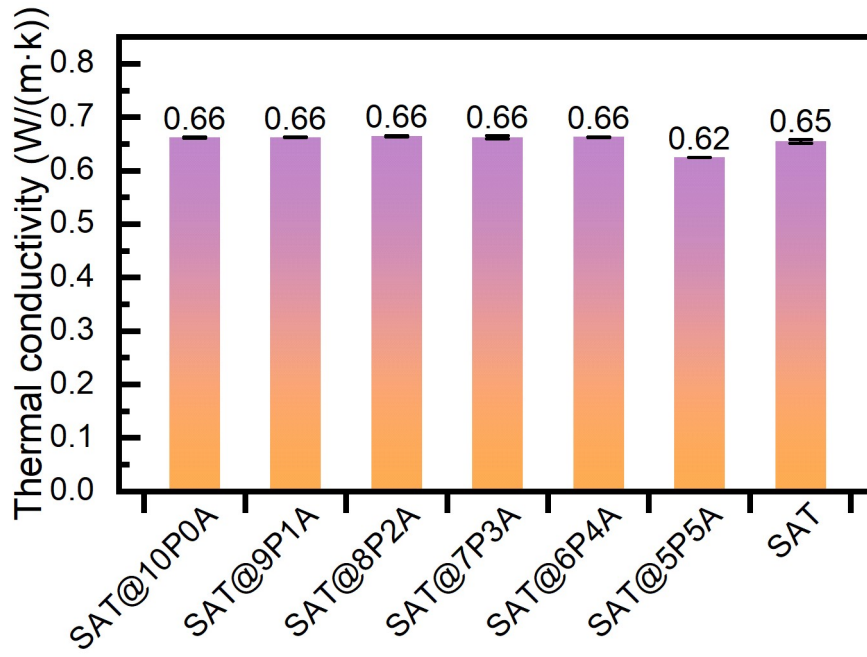
Supplementary Fig. 1 | Schematic Diagram of Hydrogel and Phase Change Gel Preparation.



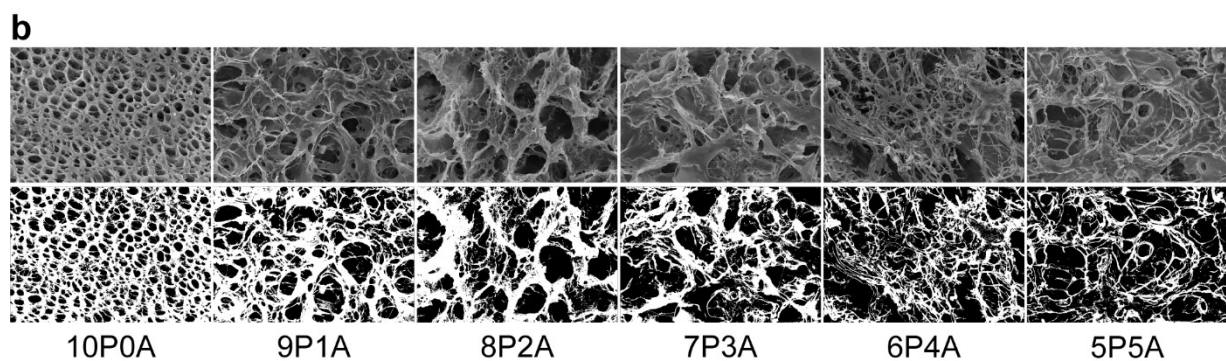
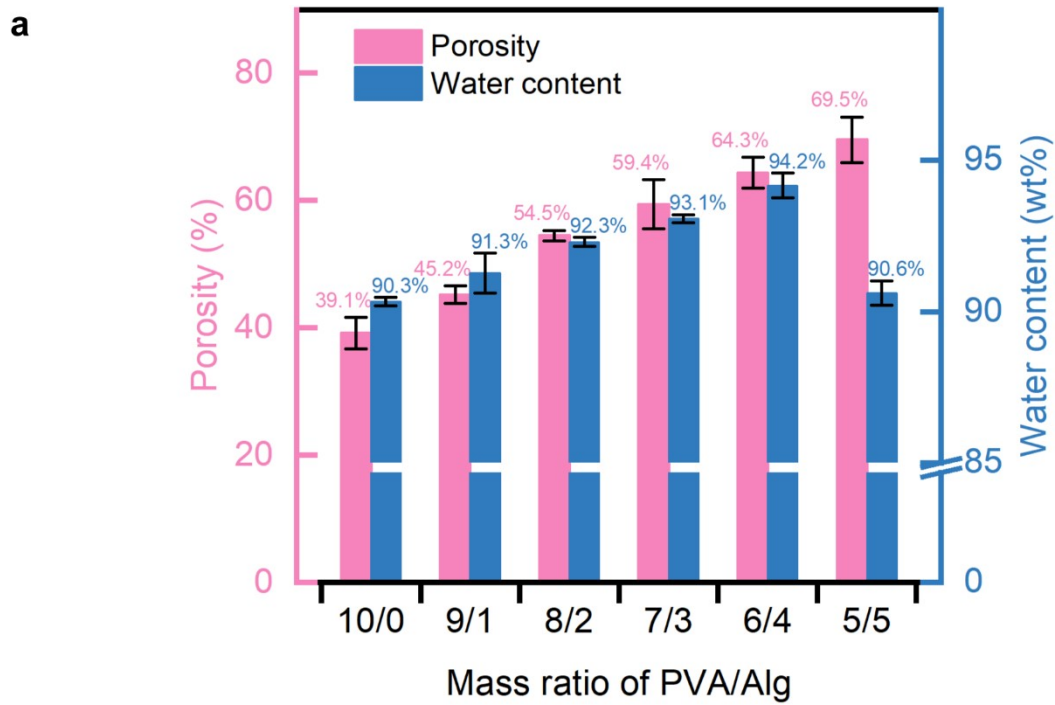
Supplementary Fig. 2 | Shape stability and leak resistance of PCGs with varied PVA/Alg ratios.



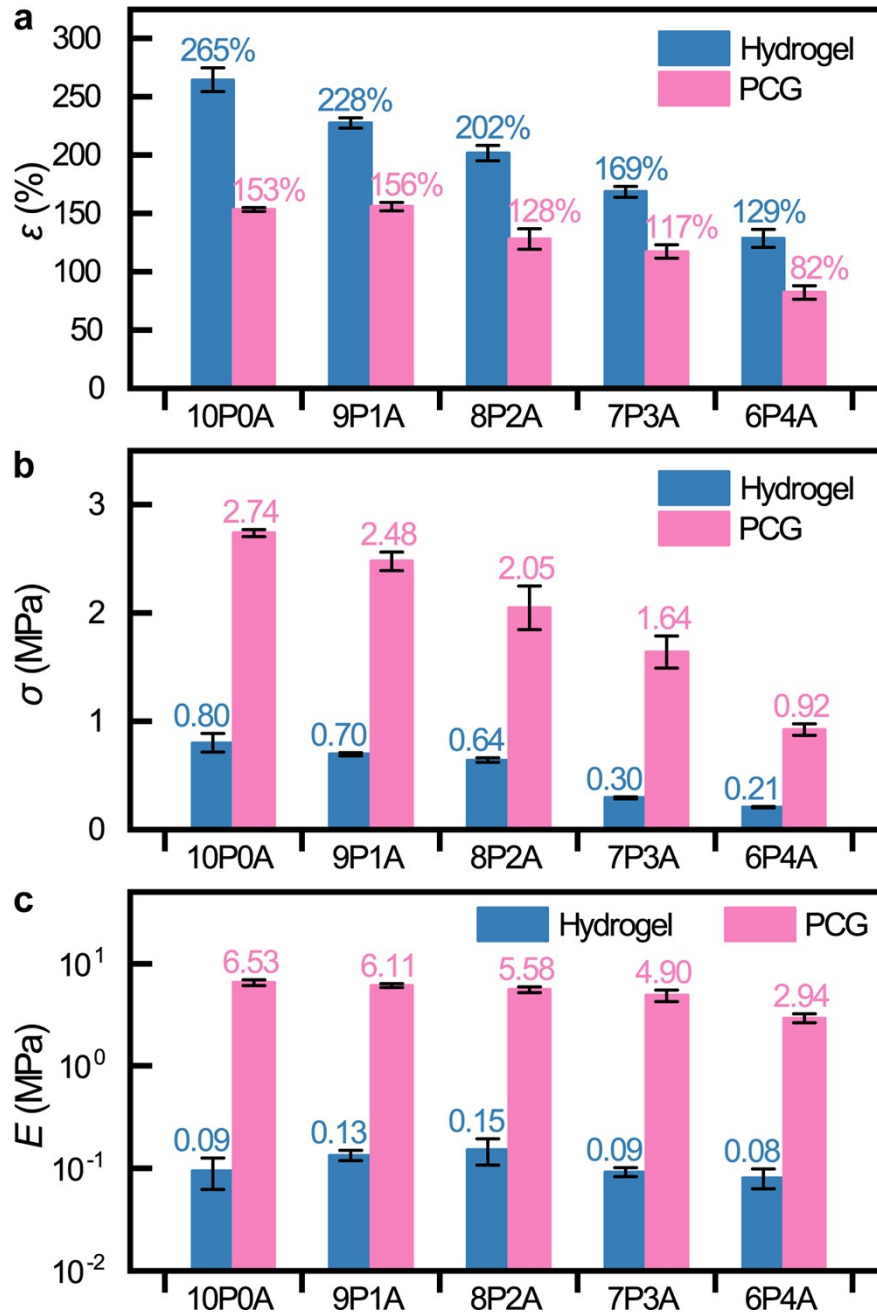
Supplementary Fig. 3 | Microstructure of hydrogel and corresponding PCGs with various PVA/Alg ratios. Low magnification (1st row) and high magnification (2nd row) SEM images of Hydrogel 10P0A (1st column), Hydrogel 8P2A (2nd column), and Hydrogel 5P5A (3rd column), along with SEM images of corresponding PCGs (3rd row).



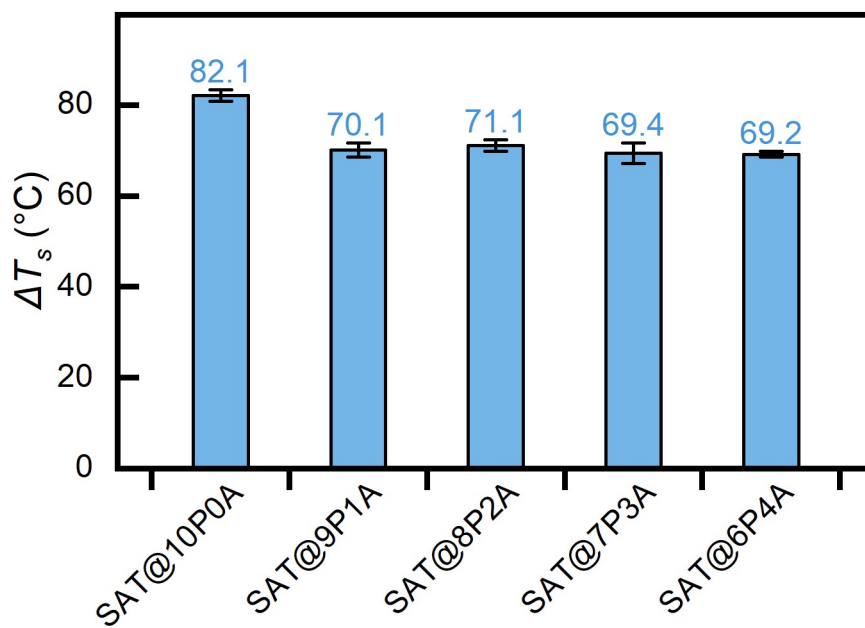
Supplementary Fig. 4 | Thermal conductivity of PCGs with various PVA/Alg ratios.



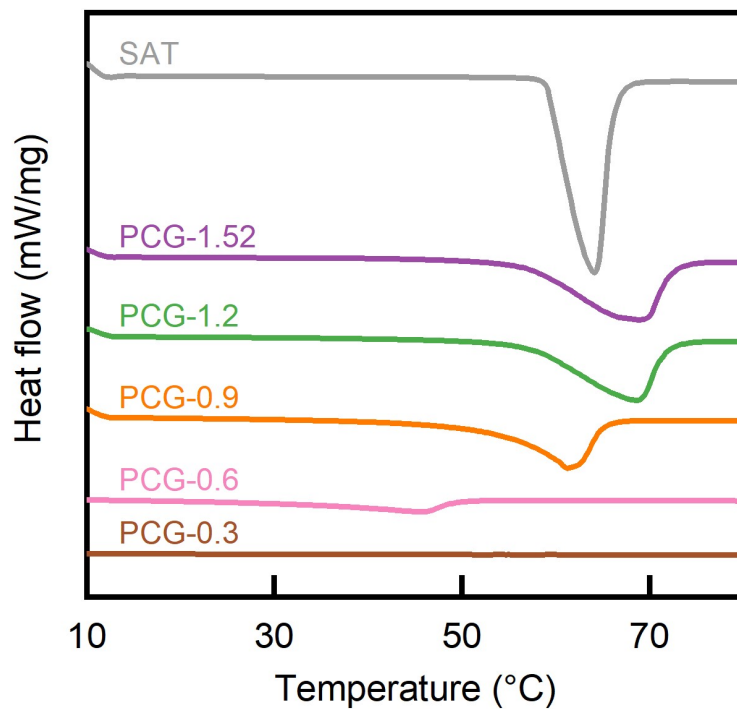
Supplementary Fig. 5 | Porosity and water content of hydrogels with various PVA/Alg ratios. a, Porosity and water content. **b,** SEM images of the hydrogel samples used for porosity calculation, shown before (1st row) and after (2nd row) processing with ImageJ. The black areas represent the pores of the polymer networks. Scale bar: 20 μm .



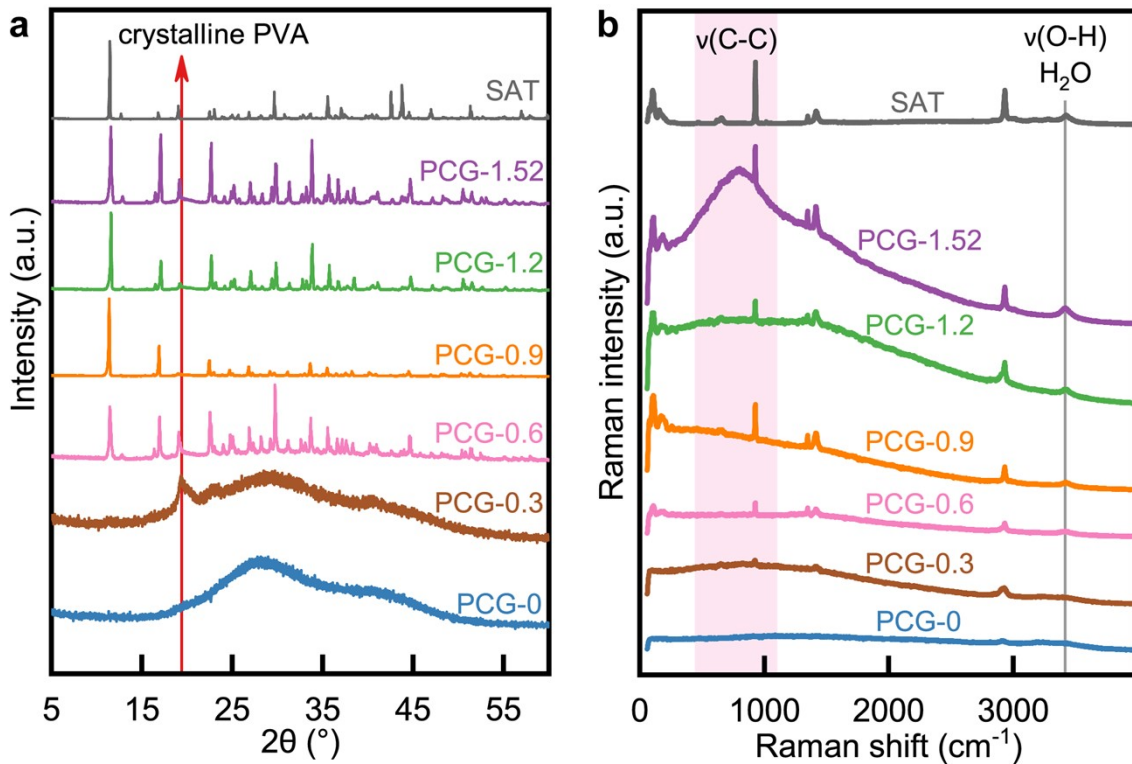
Supplementary Fig. 6 | Mechanical properties of PCGs with varying PVA/Alg ratios compared to hydrogel. a, Elongation at break (ϵ), **b**, tensile Strength (σ), and **c**, Young's modulus (E) of hydrogels and supercooled PCGs. Error bars represent the standard deviation from three samples.



Supplementary Fig. 7 | Supercooling degree of PCGs with various PVA/Alg ratios.



Supplementary Fig. 8 | DSC curves of PCGs with various R . The figure shows there is no endothermic peak in the curve of PCG-0.3, indicating that no SAT is formed in the network when $R = 0.3$.

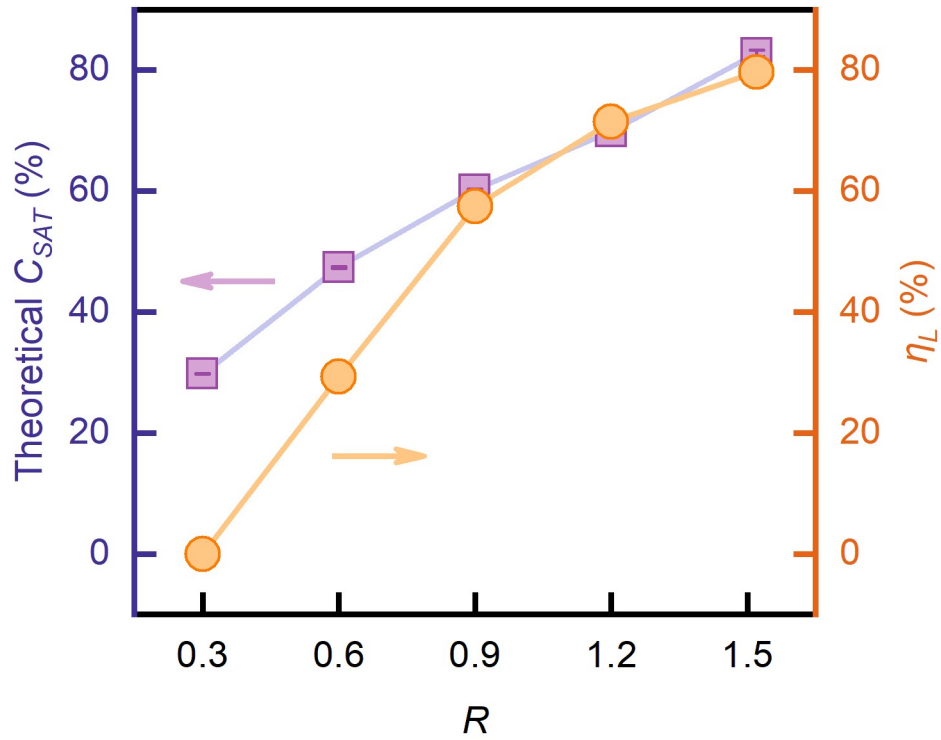


Supplementary Fig. 9 | Structure and composition of PCGs. **a**, XRD patterns and **b**, Raman spectra of SAT and PCGs with various R .

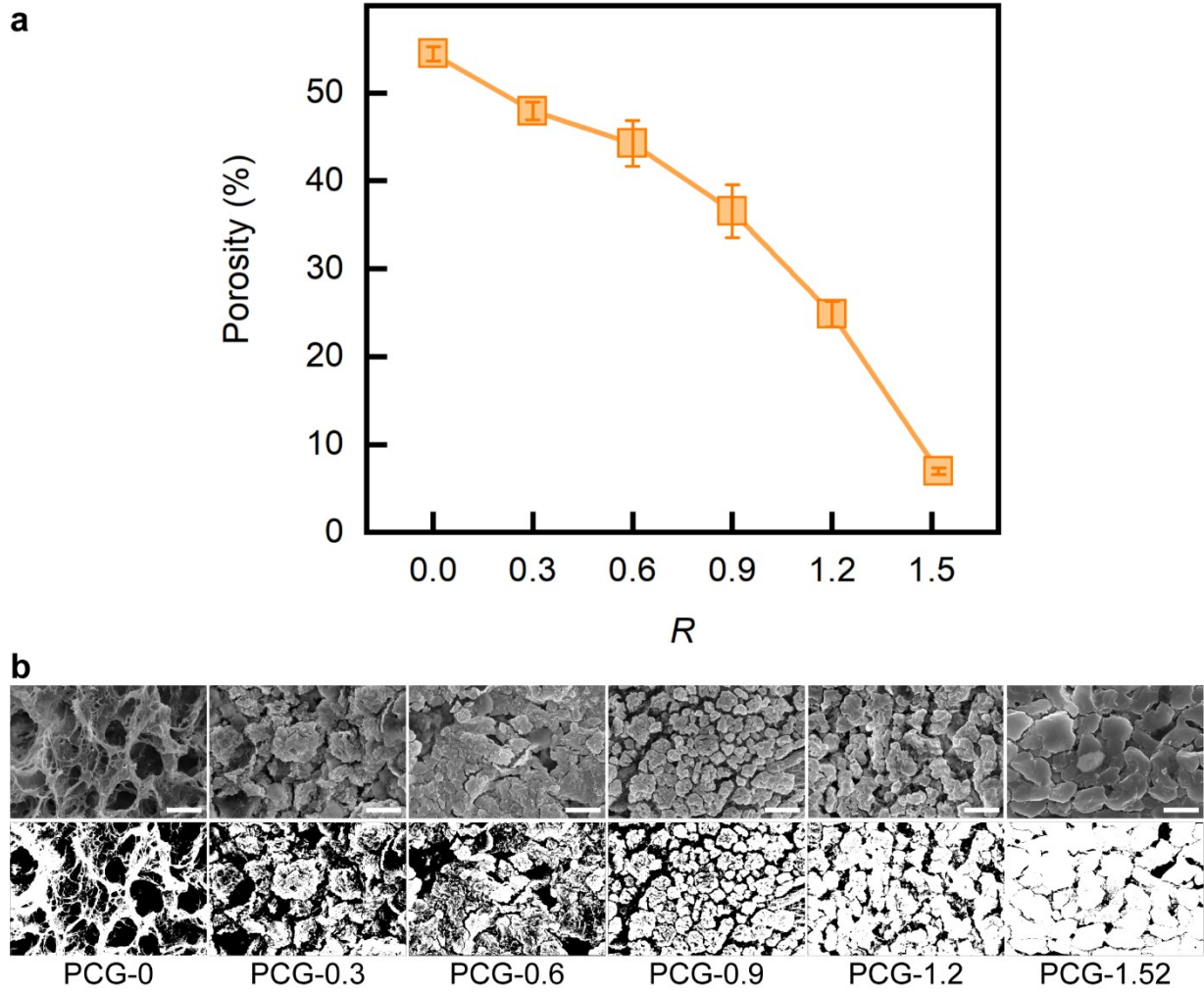
I. No diffraction peaks or characteristic peaks of SAT were observed in the XRD pattern and Raman spectrum of PCG-0.3, suggesting that no SAT forms when R is too low.

II. A distinct diffraction peak of crystalline PVA is observed in the XRD patterns of PCGs containing salt ions compared to hydrogel (PCG-0) and SAT, indicating an increase in the crystallization regions of the PVA network after pickling.

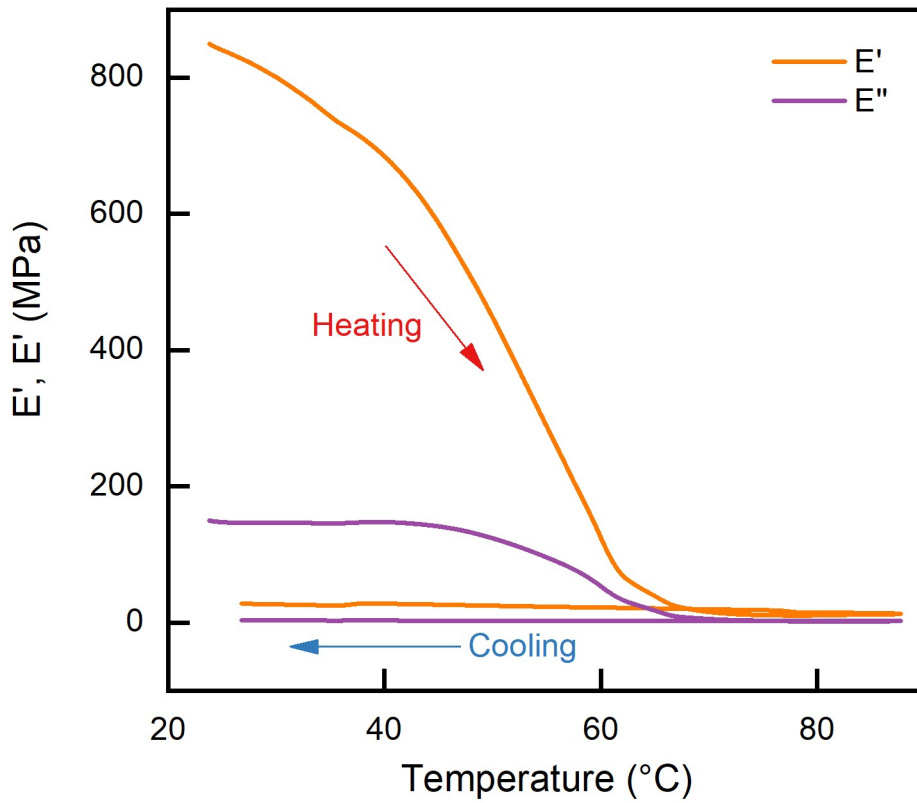
III. The Raman spectra of PCGs containing salt ions exhibit a pronounced peak corresponding to the stretching vibration of the C–C bond in the hydrogel's carbon backbone, which intensifies with increasing R , demonstrating a denser hydrogel network.



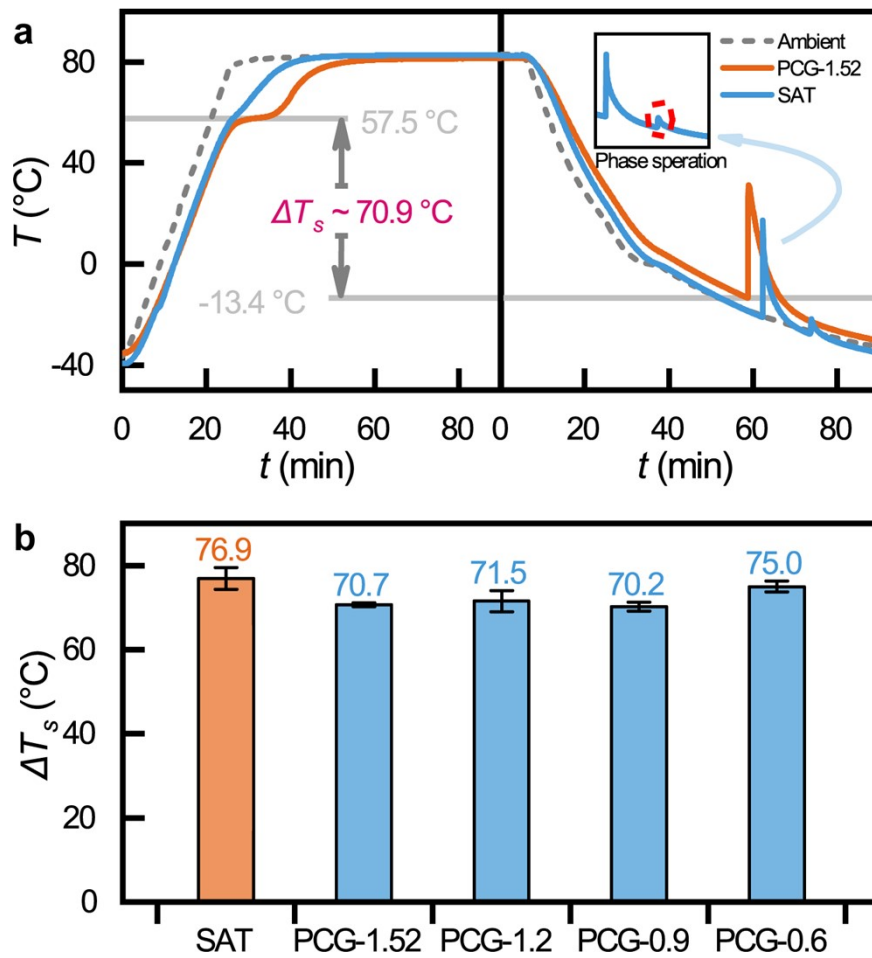
Supplementary Fig. 10 | Theoretical content of SAT (C_{SAT}) in PCGs and loading rate (η_L) of PCGs with various R . When $R \leq 0.6$, η_L calculated from enthalpy obtained from the DSC test is lower than the theoretical C_{SAT} .



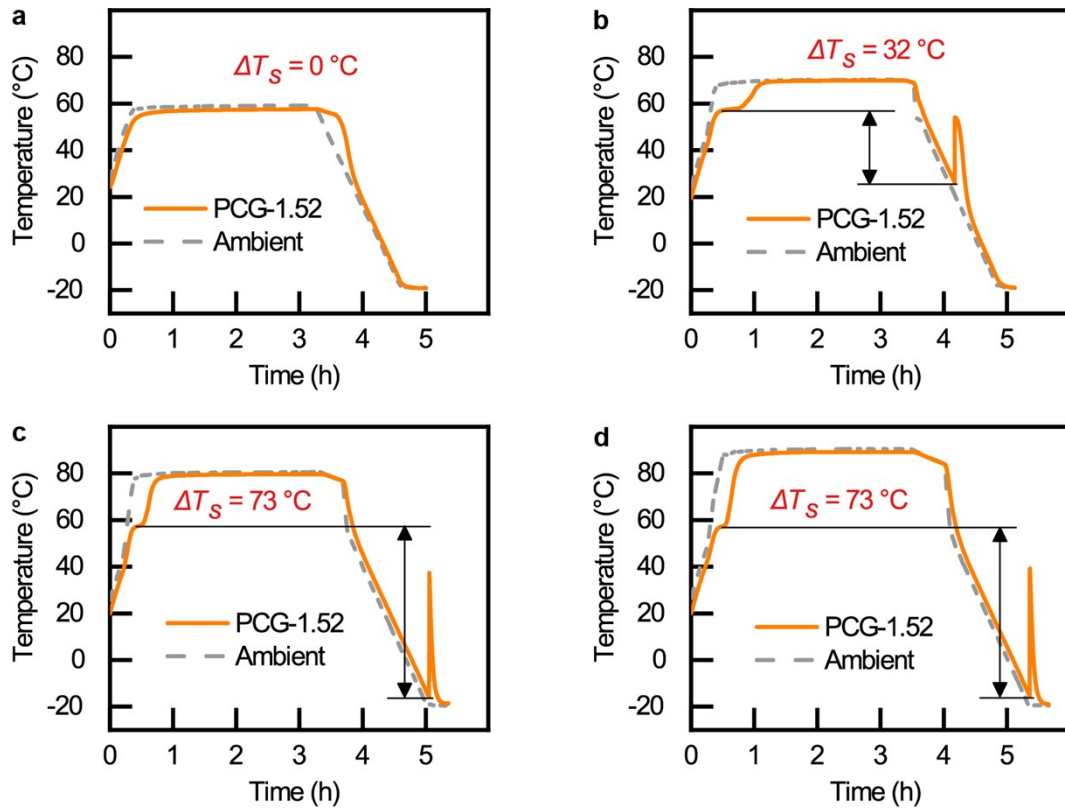
Supplementary Fig. 11 | Porosity of PCGs with different R . **a**, Porosity. **b**, SEM images of the PCG samples used for porosity calculation, shown before (1st row) and after (2nd row) processing with ImageJ. The black areas represent the pores within the PCGs. Scale bar: 20 μm for PCG-0 and 4 μm for the other samples.



Supplementary Fig. 12 | Storage modulus (E') and loss modulus (E'') of PCG-1.52 measured at a frequency of 1 Hz, with a heating-cooling rate of 2 °C/min. During the heating process, the moduli decrease sharply around 58 °C, whereas during the cooling process, the moduli exhibit only slight changes.

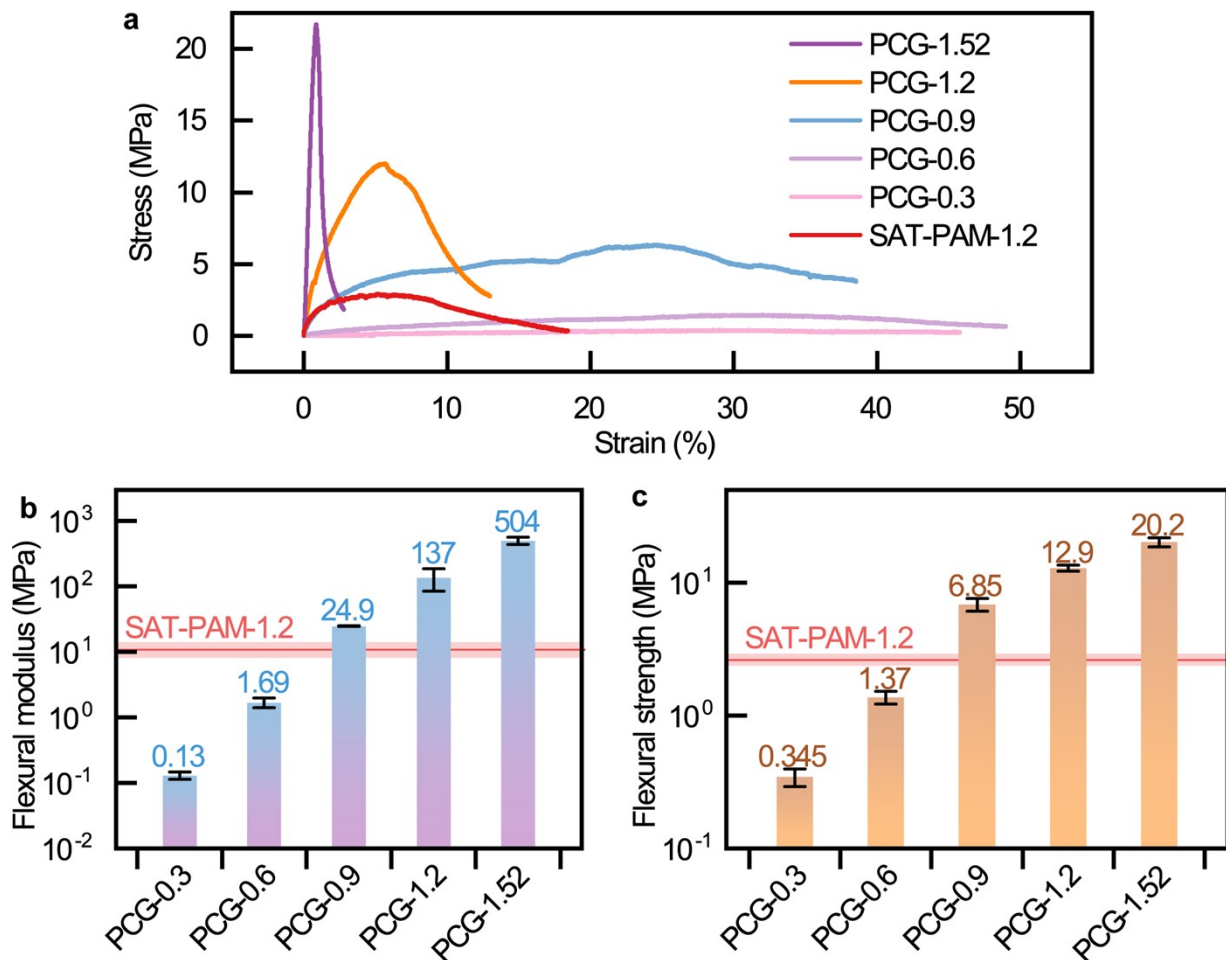


Supplementary Fig. 13 | Supercooling characteristics of SAT and PCGs. a, Heating and step cooling curves of SAT and PCG-1.52. The step cooling curve of SAT shows two exothermic peaks due to its phase separation. **b,** Supercooling degree of SAT and PCGs with various R.

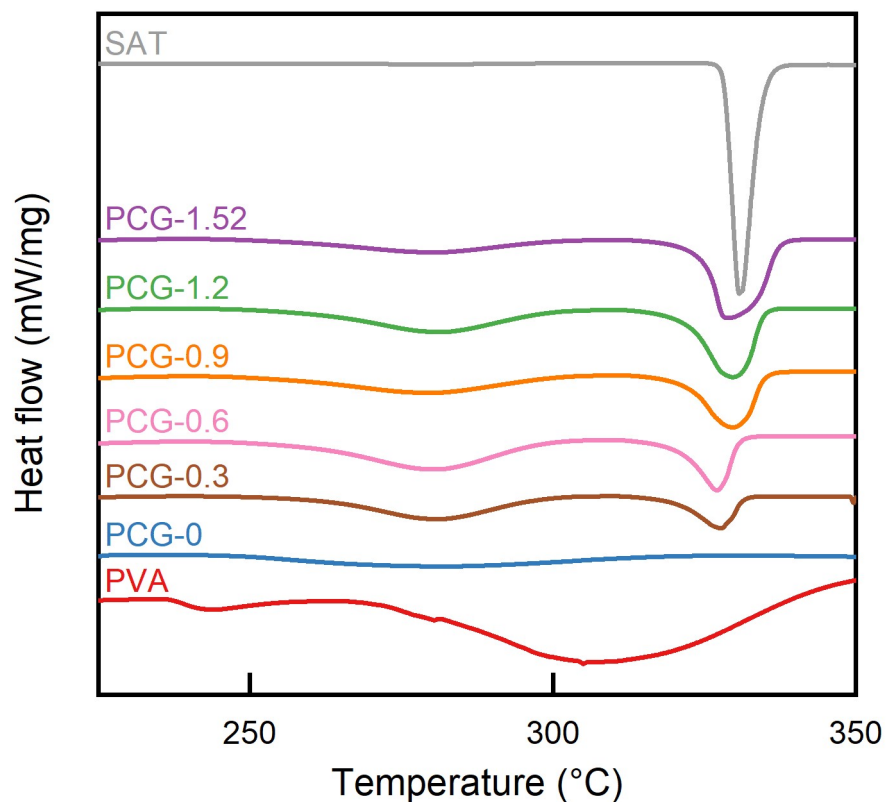


Supplementary Fig. 14 | Influence of processing parameters on the degree of supercooling.

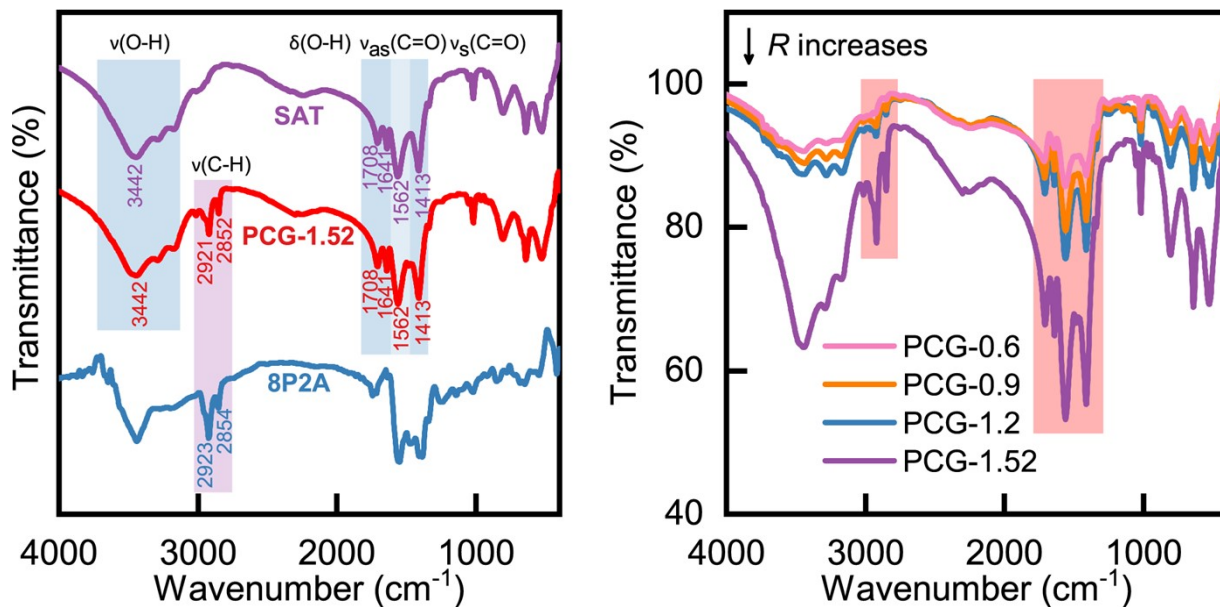
a-d, T-history curves of PCGs heated at 60 (a), 70 (b), 80 (c), and 90 °C (d), respectively, along with the corresponding ΔT_s values.



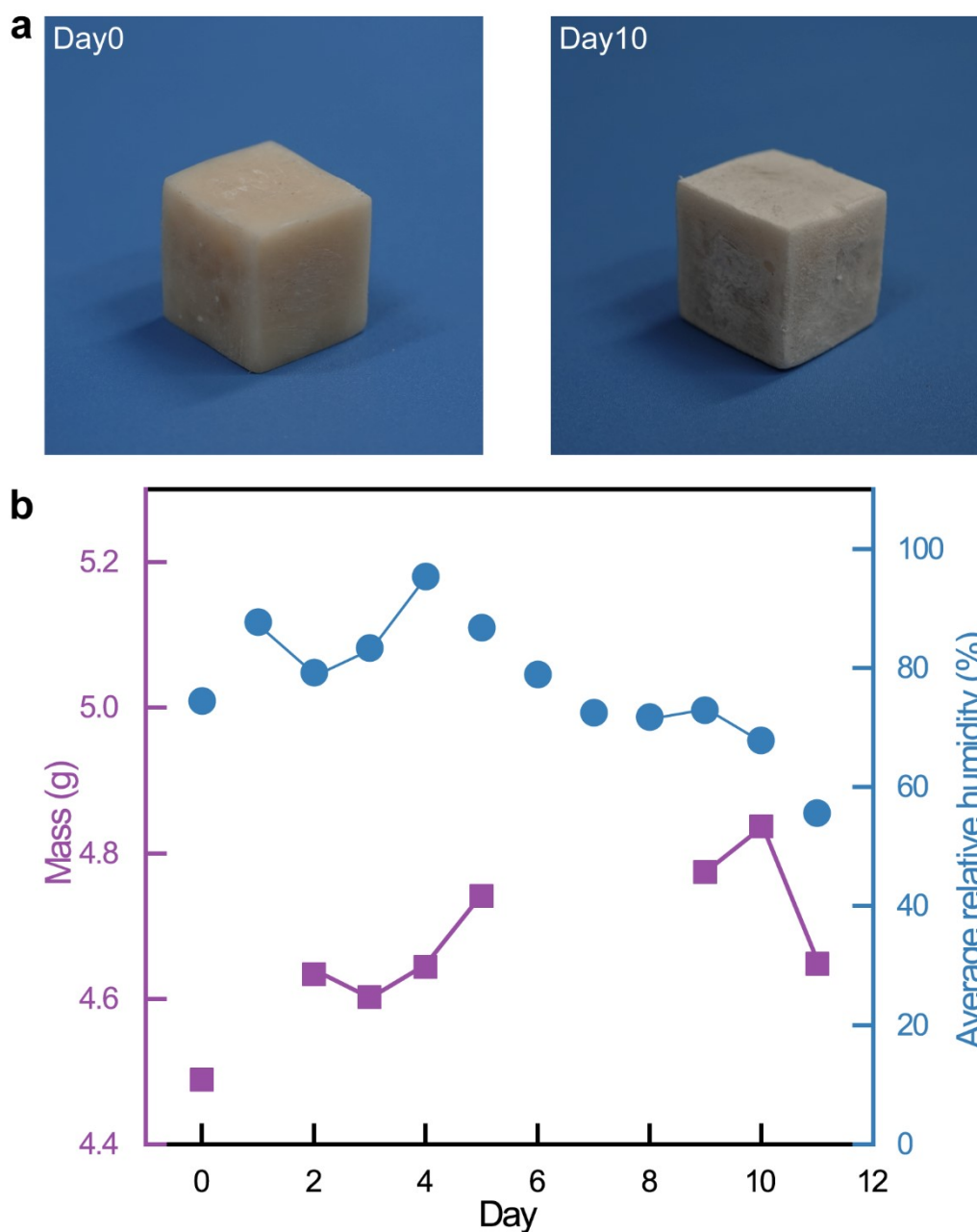
Supplementary Fig. 15 | Three-point bending tests of PCGs and SAT-PAM-1.2. **a**, Stress-strain curves. **b**, flexural modulus. **c**, flexural strength. The flexural modulus and strength of SAT-PAM-1.2 are 11.04 ± 3.17 MPa and 2.61 ± 0.27 MPa, respectively, which fall between those of PCG-0.6 and PCG-0.9 but are significantly lower than those of PCG-1.2.



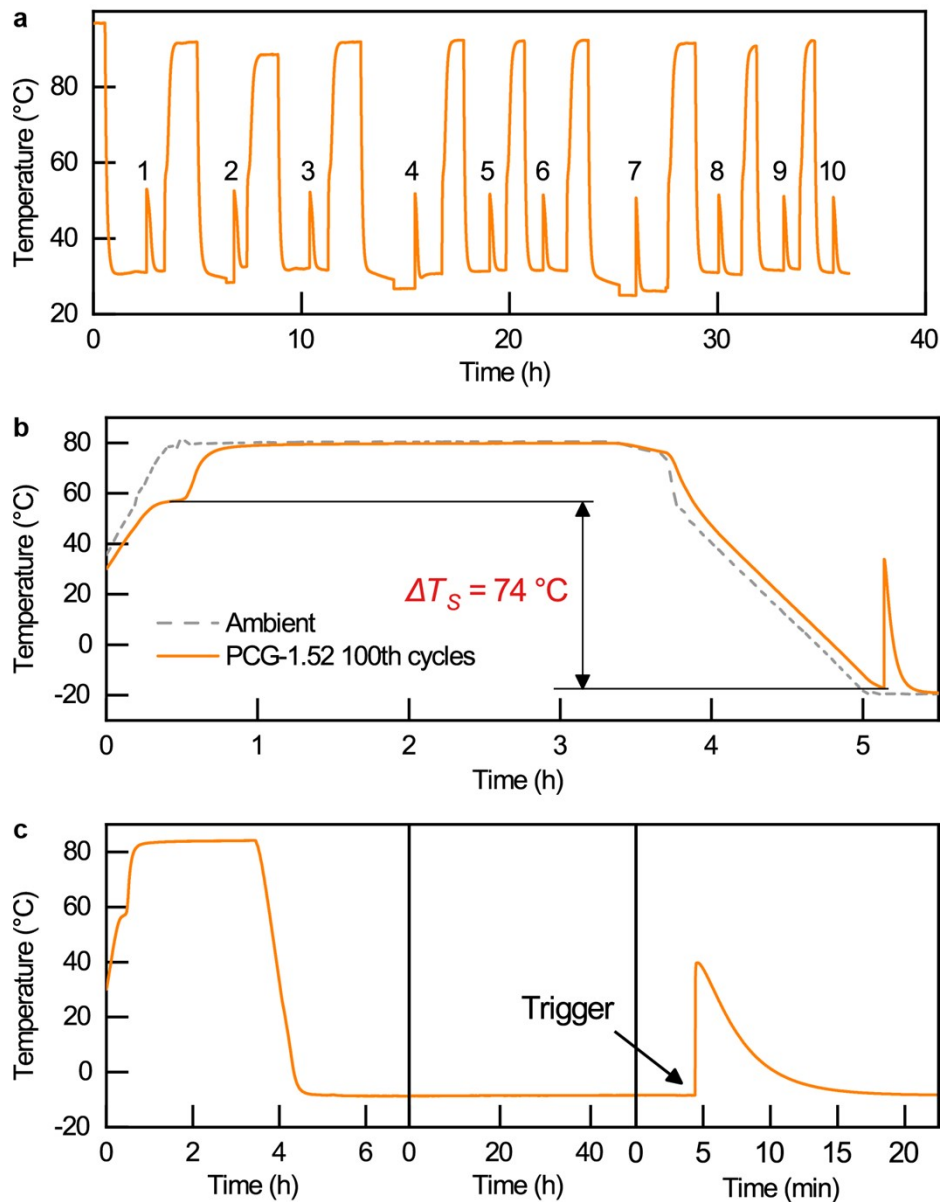
Supplementary Fig. 16 | DSC curves of SAT, PVA, and PCGs with varying R values from 225 °C to 350 °C. For PCGs, the peaks observed between 250 °C and 300 °C correspond to the melting of PVA, while the peaks between 320 °C and 340 °C indicate the decomposition process of SA.



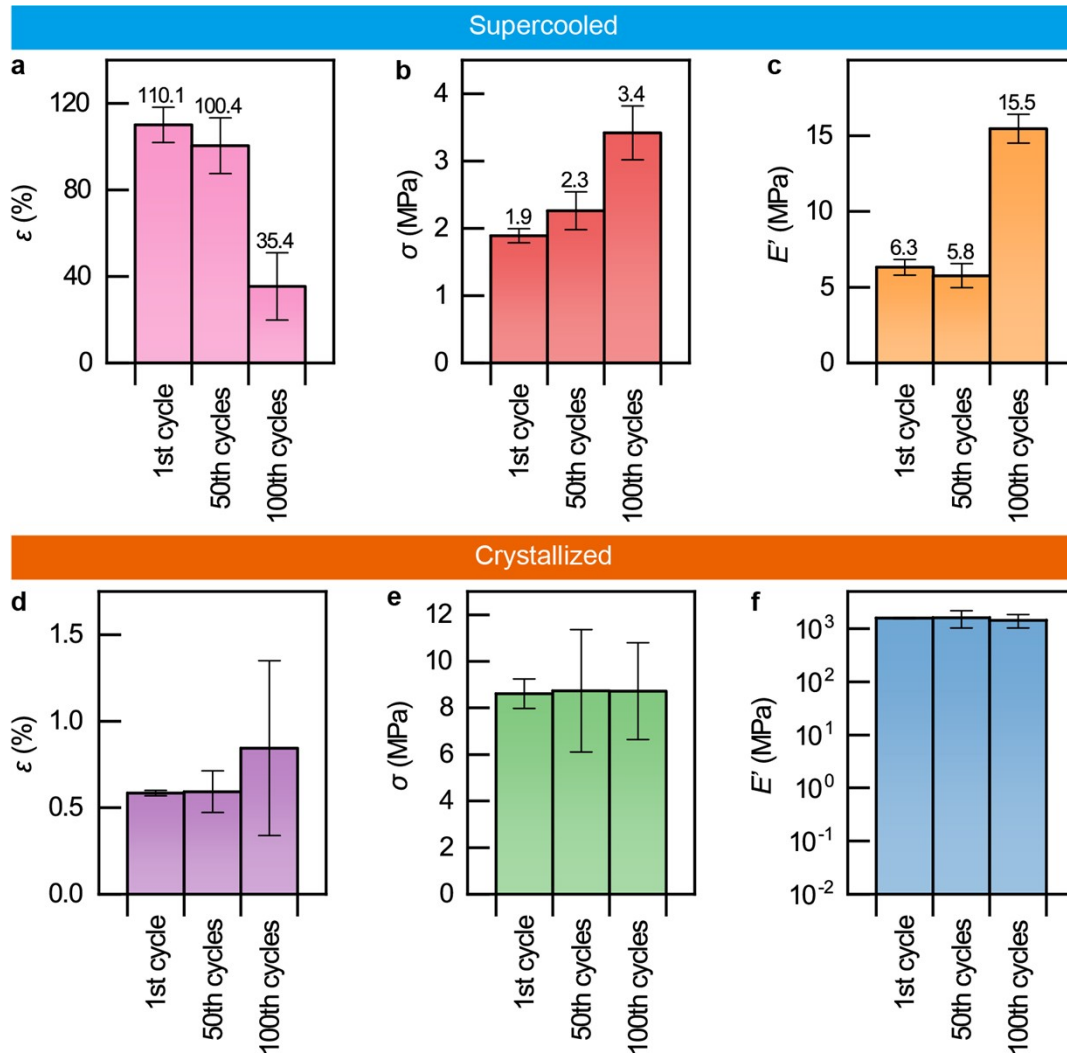
Supplementary Fig. 17 | FT-IR spectra of SAT, Aerogel 8P2A, and PCGs with various *R*.



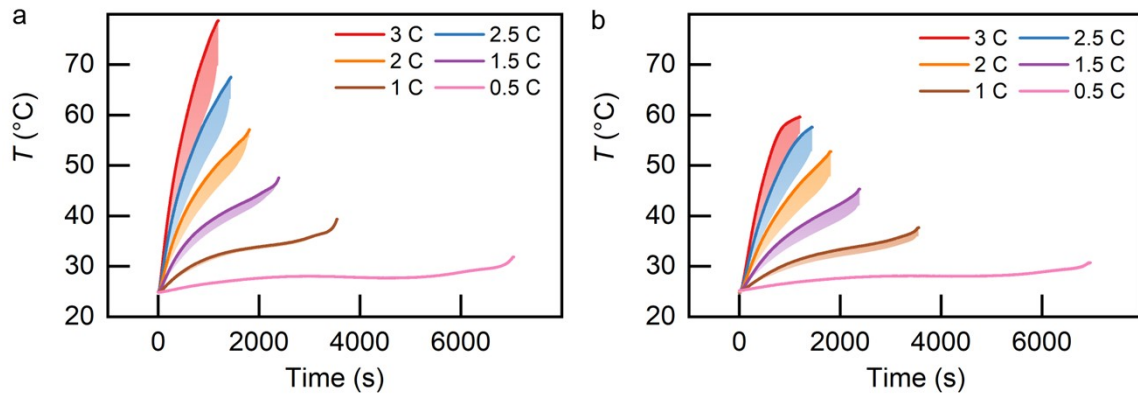
Supplementary Fig. 18 | Stability of PCG-1.52 at room temperature. a, Photos of PCG-1.52 just after preparation (left) and after 10 days of air exposure (right), showing slight salt precipitation on the surface. **b,** Mass of PCG-1.52 and the average relative humidity over several days. The mass of the PCG follows a similar trend to the changes in humidity.



Supplementary Fig. 19 | Reproducibility of mechanical triggering and supercooling performance of PCG-1.52 after 100 freeze-thaw cycles. a, PCGs over continuously 10 times heat-cool-trigger cycle using a needle tip. b, T-history curves of PCG-1.52 after 100 freeze–thaw cycles (heating to 80 °C and cooling to –20 °C), showing a consistent supercooling degree (ΔT_s) of ~74 °C. c, The sample was heated to 80 °C for 3 h, cooled to –10 °C, and maintained at that temperature for 50 h. It remained in a supercooled state and was successfully crystallized upon a single needle-tip trigger.



Supplementary Fig. 20 | Changes in mechanical properties after 50 and 100 melting/recrystallization cycles. a-c, Tensile strain (a), tensile stress (b), and Young's modulus (c) of PCG-1.52 at the supercooled state after the 1st, 50th, and 100th cycles. d-f, Tensile strain (d), tensile stress (e), and Young's modulus (f) of PCG-1.52 at the crystallized state after the 1st, 50th, and 100th cycles.



Supplementary Fig. 21 | Lithium-ion battery thermal management performance of PCG-1.52. a, b, Temperature rise profiles of the control (a) and PCG-integrated (b) battery packs under various discharge rates. Shaded areas represent the temperature difference between the hottest and coldest cells within each pack.

Supplementary Table 1 Mass percentage of components in hydrogels with different PVA/Alg ratios and their water content.

Samples	H₂O (wt%)	PVA (wt%)	Alg (wt%)	C_{H_2O} (%)
10P0A	90	10	0	90.3
9P1A	90	9	1	91.3
8P2A	90	8	2	92.3
7P3A	90	7	3	93.1
6P4A	90	6	4	94.2
5P5A	90	5	5	90.6

Supplementary Table 2 Melting point (T_m) and melting enthalpy (ΔH_m) of SAT and PCGs with various PVA/Alg ratios.

Sample	T_m (°C)	ΔH_m (kJ/kg)
SAT	58.6 ± 0.3	264.1 ± 4.4
SAT@10P0A	58.1 ± 0.6	198.7 ± 8.4
SAT@9P1A	57.1 ± 0.3	205.3 ± 2.8
SAT@8P2A	57.2 ± 0.3	210.3 ± 8.7
SAT@7P3A	57.8 ± 1.2	216.8 ± 2.9
SAT@6P4A	56.8 ± 0.3	222.6 ± 3.3
SAT@5P5A	56.7 ± 0.6	209.8 ± 10.7

Noted: The standard deviation was calculated from three samples. The solidification enthalpy was not present because SAT and PCGs have high supercooling degrees and exceed the detecting range of the instrument (see **Supplementary Fig. 7** and **Supplementary Fig. 13**).

Supplementary Table 3 The melting enthalpy of PCGs with various PVA/Alg ratios before (ΔH_m) and after ($\Delta H_{m, 100th}$) undergoing 100 thermal cycles, and the corresponding loss rate (L).

Sample	ΔH_m (kJ/kg)	$\Delta H_{m, 100th}$ (J/g)	L (%)
SAT@10P0 A	198.7	169.8	14.5
SAT@9P1A	205.3	200.3	2.4
SAT@8P2A	210.3	204.9	2.6
SAT@7P3A	216.8	211.7	2.4
SAT@6P4A	222.6	218.0	2.1

Noted: The standard deviation was calculated from three samples.

Supplementary Table 4 Summary of form-stable hydrated salt phase change gels

Literature	Salt	Hydrogel network	Method	ΔH_m (kJ/kg)	η (%)	Mechanical performance
This work	SAT	PVA/Alg	Ion permeation	210.3	79.6	Tensile: Soft: $\sigma=2.05$ MPa $E=5.58$ MPa Rigid: $\sigma=8.79$ MPa $E=2120$ MPa
1 Wang, T., et al. Preparation and properties of a form-stable phase-change hydrogel for thermal energy storage. <i>J of Applied Polymer Sci</i> 133, app.43836 (2016).	SSD	PAM/CA	In situ synthesis	202.9	80.8	Tensile: $\sigma\sim 0.05$ MPa $E\sim 0.72$ MPa
2 Yang, F. (Kuo), Cholewinski, A., et al. A hybrid material that reversibly switches between two stable solid states. <i>Nat. Mater.</i> 18, 874–882 (2019).	SAT	PAA	In situ synthesis	N/A	N/A	Indentation: Soft: $E=0.015$ MPa Rigid: $E=385$ MPa
3 Jing, H., et al. A phase-change gel-based pressure sensor with tunable sensitivity for artificial tactile feedback systems. <i>J. Mater. Chem. A</i> 9, 19914–19921 (2021).	CCH	PAM	In situ synthesis	N/A	N/A	Compression: Soft: $E=0.30$ MPa Rigid: $E=342$ MPa
4 Yin, C. et al. Shape-Stable Hydrated Salts/Polyacrylamide Phase-Change Organohydrogels for Smart Temperature Management. <i>ACS Appl. Mater. Interfaces</i> 13, 21810–21821 (2021).	DPD H	PAM	In situ synthesis	115.9	48.6	Compression: $E\sim 0.08$ MPa
5 Luo, Y. et al. Self-healing inorganic hydrated salt gels for personal thermal management in the static and dynamic modes. <i>Chemical Engineering Journal</i> 440, 135632 (2022).	SSD	PAAS/CA	In situ synthesis	147.1	62.2	Tensile: $\sigma=0.053$ MPa $E\sim 0.38$ MPa
6 Fang, Y. et al. Phase Change Hydrogels for Bio-Inspired Adhesion and Energy Exchange Applications. <i>Adv Funct Materials</i> 33, 2301505 (2023).	SAT	PAM	In situ synthesis	N/A	N/A	Tensile: Rigid: $\Sigma\sim 2.0$ MPa $E\sim 340.7$ MPa
7 Qi, X. et al. Multifunctional polyacrylamide/hydrated salt/MXene phase change hydrogels with high thermal energy storage, photothermal conversion capability and strain sensitivity for personal healthcare. <i>Composites Science and Technology</i> 234, 109947 (2023).	SSD	PAM	In situ synthesis	163.3	58.0	Compression: $E\sim 0.14$ MPa
8 Song, M. et al. Thermally induced flexible phase change hydrogels for solar thermal storage and human thermal management. <i>Chemical Engineering Journal</i> 464, 142682 (2023).	SAT	KGM/PAM	In situ synthesis	179.2	70.5	Compression: Soft: $E\sim 0.07$ MPa Rigid: $E\sim 14.3$ MPa
9 Zhu, T. et al. MXene/Ag doped hydrated-salt hydrogels with excellent thermal/light energy storage, strain sensing and photothermal antibacterial performances for intelligent human healthcare. <i>Composites Part A: Applied Science and Manufacturing</i> 170, 107526 (2023).	SSD	PAM/CA	In situ synthesis	176.0	65.0	Tensile: $\sigma\sim 0.15$ MPa $E\sim 0.017$ MPa
10 Fang, Y. et al. Reversible Phase Change-Induced Hardening and Softening for Conditions-Adaptive and Mechanics-Reconfigurable Applications. <i>Adv Funct Materials</i> 2314353 (2024) doi:10.1002/adfm.202314353.	SAT	PAM	In situ synthesis	N/A	N/A	Compression: Soft: $E\sim 0.1$ MPa Rigid: $E\sim 24.0$ MPa

11	Wei, J. et al. Dissolution–Crystallization Transition within a Polymer Hydrogel for a Processable Ultratough Electrolyte. <i>Adv. Mater.</i> 31, 1900248 (2019).	SAT	PAM	In situ synthesis	N/A	N/A	Compression: Rigid: $E \sim 474.24$ MPa
12	Liu, Q., Fang, Y., Xiong, X., Xu, W. & Cui, J. Ostwald ripening for designing time-dependent crystal hydrogels. <i>Angewandte Chemie International Edition</i> 63, e202320095 (2024).	SAT	PAM	In situ synthesis	N/A	N/A	Compression: Soft: $E \sim 0.04$ MPa Rigid: $E \sim 7.2$ MPa
13	Schroeder, T. B. H. & Aizenberg, J. Patterned crystal growth and heat wave generation in hydrogels. <i>Nat Commun</i> 13, 259 (2022).	SAT	PAM	In situ synthesis	N/A	N/A	N/A

Note: $\eta = (\Delta H_m \text{ of PCG}) / (\Delta H_m \text{ of pure hydrated salt}) \times 100\%$; SSD: sodium sulfate decahydrate, CCH: calcium chloride hexahydrate, DPDH: disodium phosphate dodecahydrate, PAM: polyacrylamide, CA: calcium alginate, PAA: polyacrylic acid, PAAS: sodium polyacrylate, KGM: konjac glucomannan.

Supplementary Table 5 | Melting point ($T_{m, PVA}$) and melting enthalpy ($\Delta H_{m, PVA}$) of PVA, and decomposition point ($T_{d, SA}$) and decomposition enthalpy ($\Delta H_{d, SA}$) of SA in PCGs with varying R values.

Sample	$T_{m, PVA}$	$\Delta H_{m, PVA}$	$T_{d, SA}$	$\Delta H_{d, SA}$
PCG-0	247.19	62.97	N/A	N/A
PCG-0.3	260.49	72.86	32.54	319.77
PCG-0.6	259.39	96.69	48.33	318.22
PCG-0.9	253.36	65.62	67.06	321.87
PCG-1.2	258.43	79.02	82.68	321.89
PCG-1.52	253.69	48.45	101	324.76
SAT	N/A	N/A	121.7	328.26
PVA	277.32	492.4	N/A	N/A

Supplementary Table 6 | Addition amount of each substance in the preparation process of phase change gels (PCGs) with different mass ratios of SA to H₂O (*R*).

Sample	Hydrogel 8P2A		SA Solution		Total mass of H ₂ O	<i>R</i>
	Total mass (g)	Mass of H ₂ O in the hydrogel (g)	Mass of SA (g)	Mass of H ₂ O		
PCG-0	20.00	18.46	0.00	81.54	100.00	0.00
PCG-0.3	20.00	18.46	30.00	81.54	100.00	0.30
PCG-0.6	20.00	18.46	60.00	81.54	100.00	0.60
PCG-0.9	20.00	18.46	90.00	81.54	100.00	0.90
PCG-1.2	20.00	18.46	120.00	81.54	100.00	1.20
PCG-1.52	20.00	18.46	152.00	81.54	100.00	1.52

Supplementary Table 7 | Thermal and mechanical properties of PCG-1.52 prepared with different freeze–thaw cycles.

Properties	1 cycle	3 cycles
Freeze-thaw time (h)	12	36
Enthalpy (kJ/kg)	222.0 ± 6.2	210.3 ± 8.7
Strain (%)	110.07 ± 8.11	128.09 ± 8.78
Stress (MPa)	1.89 ± 0.11	2.05 ± 0.20
Young's Modulus (MPa)	6.31 ± 0.51	5.58 ± 0.35

Description of Supplementary Videos

Supplementary Video 1 | Phase Transitions of PCGs Triggered by Touch

Supercooled PCGs undergo phase transitions and release heat upon finger touch. From the infrared camera's view, the crystallized region gradually expands outward from the contact point, and the 35 °C thermochromic pigment applied to the surface changes color, continuing until the entire material has crystallized.

Supplementary Video 2 | Hammer Test

Pure SAT, PAM (SAT-PAM-1.2) using the one-pot method, and our PCG-1.2 are subjected to hammering. Pure SAT are easily crushed, while SAT-PAM-1.2 is flattened. In contrast, PCG-1.2 maintains its shape with only minor surface scratches.

Supplementary Video 3 | Hydrophobicity of Superhydrophobic Surface.

The Superhydrophobic Surface (SHS) exhibits excellent hydrophobicity at normal temperatures. When it is placed on a 10° inclined platform at 25 °C, water droplets falling on it rebound at an angle and quickly slide off the surface. However, at a low temperature of -10 °C, the water droplets adhere to its surface.

Supplementary Video 4 | Deicing Experiment.

A 2 mm-thick sheet of PCG-1.52 with a Superhydrophobic Surface (SHS) was placed on a 10° inclined platform at -10 °C with an ice droplet adhered to it. When the PCG was triggered with a needle, its temperature dramatically increased to 43 °C. The heat release from the PCG melted the bottom of the ice droplet, causing it to finally slide off the surface.

References

- 1 C. M. Hassan and N. A. Peppas, *Macromolecules*, 2000, **33**, 2472–2479.
- 2 C. Yang and Z. Suo, *Nat Rev Mater*, 2018, **3**, 125–142.